

## Comparison of 3D orientation distribution functions measured with confocal microscopy and diffusion MRI

Kurt Schilling <sup>a,b,\*</sup>, Vaibhav Janve <sup>a,b</sup>, Yurui Gao <sup>a,b</sup>, Iwona Stepniewska <sup>c</sup>, Bennett A. Landman <sup>a,b,d</sup>, Adam W. Anderson <sup>a,b</sup>

<sup>a</sup> Vanderbilt University Institute of Imaging Science, Vanderbilt University, Nashville, TN, USA

<sup>b</sup> Department of Biomedical Engineering, Vanderbilt University, Nashville, TN, USA

<sup>c</sup> Department of Psychology, Vanderbilt University, Nashville, TN, USA

<sup>d</sup> Department of Electrical Engineering, Vanderbilt University, Nashville, TN, USA



### ARTICLE INFO

#### Article history:

Received 9 October 2015

Accepted 11 January 2016

Available online 21 January 2016

#### Keywords:

Diffusion MRI

Validation

Fiber orientation distribution

DTI

Crossing fibers

### ABSTRACT

The ability of diffusion MRI (dMRI) fiber tractography to non-invasively map three-dimensional (3D) anatomical networks in the human brain has made it a valuable tool in both clinical and research settings. However, there are many assumptions inherent to any tractography algorithm that can limit the accuracy of the reconstructed fiber tracts. Among them is the assumption that the diffusion-weighted images accurately reflect the underlying fiber orientation distribution (FOD) in the MRI voxel. Consequently, validating dMRI's ability to assess the underlying fiber orientation in each voxel is critical for its use as a biomedical tool. Here, using post-mortem histology and confocal microscopy, we present a method to perform histological validation of orientation functions in 3D, which has previously been limited to two-dimensional analysis of tissue sections. We demonstrate the ability to extract the 3D FOD from confocal z-stacks, and quantify the agreement between the MRI estimates of orientation information obtained using constrained spherical deconvolution (CSD) and the true geometry of the fibers. We find an orientation error of approximately 6° in voxels containing nearly parallel fibers, and 10–11° in crossing fiber regions, and note that CSD was unable to resolve fibers crossing at angles below 60° in our dataset. This is the first time that the 3D white matter orientation distribution is calculated from histology and compared to dMRI. Thus, this technique serves as a gold standard for dMRI validation studies – providing the ability to determine the extent to which the dMRI signal is consistent with the histological FOD, and to establish how well different dMRI models can predict the ground truth FOD.

© 2016 Elsevier Inc. All rights reserved.

## Introduction

Diffusion magnetic resonance imaging (dMRI) has become a mainstay in neuroimaging studies due to its ability to provide, noninvasively, unique biological and clinical information about tissue composition, microstructure, and architectural organization (Basser and Pierpaoli, 1996; Beaulieu, 2002). Of particular interest is the ability to estimate the distribution of neuronal fiber orientations in each voxel from a set of diffusion measurements, an object often referred to as the fiber orientation distribution (FOD). By following these fiber orientation estimates from voxel

to voxel throughout the brain, intricate maps of brain connectivity can be created. This process of mapping brain connectivity using dMRI data has been termed “fiber tractography” (Mori et al., 1999; Mori and van Zijl, 2002), and has been used in applications ranging from delineating brain networks (Hagmann et al., 2007), to studying the changes associated with disease (Kitamura et al., 2013; Koenig et al., 2015), psychiatric disorders (White et al., 2008), and traumatic brain injury (Shenton et al., 2012).

Diffusion tensor imaging (DTI) was the first MRI method to allow mapping of fiber orientations throughout the brain (Basser et al., 1994), and remains the most common. However, this uni-modal Gaussian diffusion model is known to be inadequate for characterizing diffusion in voxels with complex fiber structure (Wiegell et al., 2000) and has been shown to lead to erroneous tractography results. A number of methods have been introduced to address this “crossing fiber” problem (Anderson, 2005; Assaf and Basser, 2005; Behrens et al., 2007; Behrens et al., 2003; Descoteaux et al., 2007; Jansons and Alexander, 2003; Ozarslan et al., 2006; Tournier et al., 2004; Tuch, 2004; Tuch et al., 2002; Wedeen et al., 2005). Typically, these

**Abbreviations:** dMRI, diffusion magnetic resonance imaging; FOD, fiber orientation distribution; DTI, diffusion tensor imaging; ODF, orientation density function; WM, white matter; GM, gray matter; CSD, constrained spherical deconvolution; SH, spherical harmonics; PSF, point spread function; ABA, adaptive bases algorithm; PPD, preservation of principal directions; SNR, signal to noise ratio.

\* Corresponding author at: Vanderbilt University Institute of Imaging Science, 1161 21st Avenue South, Medical Center North, AA-1105, Nashville, TN 37232-2310, USA.

E-mail address: [kurt.g.schilling@vanderbilt.edu](mailto:kurt.g.schilling@vanderbilt.edu) (K. Schilling).

approaches solve for the fiber orientation by estimating the FOD or the orientation density function (ODF) — another spherical function, which reflects the relative number of spins that have diffused in any given direction. Tractography algorithms then exploit local peaks in the FOD or ODF to propagate tract streamlines.

While these techniques have produced improvements in white matter tractography, there has been no clear consensus on a “gold standard” for validating the underlying orientation distributions. The most common method to date has been validation using synthetic data (Alexander, 2005; Sakaie and Lowe, 2007). However, these simulations rely on assumptions and approximations to generate the modeled MR signal, and are likely to be inadequate for validation in the living brain. Physical phantoms can be used to provide more realistic experiment conditions (including artifacts inherent to dMRI) and allow control of the ground truth orientation distribution. Yet, these capillary-based (Lin et al., 2003; Yanasak and Allison, 2006) or synthetic fiber-based (Farrher et al., 2012; Fieremans et al., 2008; Perrin et al., 2005) phantoms can still fail to replicate the structural characteristics typical of neuronal tissue, including axon diameter, membrane permeability, and most importantly, the enormous geometric complexity seen in the central nervous system.

To overcome these limitations, several studies have validated orientation measures using post-mortem histology. From stained tissue sections, techniques such as manual tracing (Leergaard et al., 2010), structure tensor analysis (Seehaus et al., 2015), and Fourier analysis (Choe et al., 2012) have been used to quantify the histological FOD. However, two potential disadvantages have plagued histological validation studies to date. First, many have been limited to two-dimensional (2D), in-plane analysis of tissue sections. Thus, they rely on tissue sectioning in a plane parallel to the direction of fibers, and analysis is restricted to only those fibers oriented in that plane. Recently, this limitation of validation studies has been circumvented through the use of confocal microscopy (Jespersen et al., 2012; Khan et al., 2015) and optical coherence tomography (Wang et al., 2015). However, no method has been presented which characterizes the full fiber orientation distribution in white matter voxels, but rather recent studies estimate a single dominant orientation in areas equivalent in size to an MRI voxel (Khan et al., 2015; Wang et al., 2015), or determine the orientation distribution in axons and dendrites of the cerebral cortex (Jespersen et al., 2012). Second, comparing MRI and histology is often done through manual alignment (Khan et al., 2015; Leergaard et al., 2010; Seehaus et al., 2013) of the data, which is prone to error and can lead to geometric mismatch and a bias in the validation results. Consequently, there is a need for a method to compare dMRI estimates of white matter pathways to direct measurements of axonal orientations on a voxel-by-voxel basis — one which allows three-dimensional (3D) analysis and addresses accurate, reproducible registration.

In this study, using post-mortem histology and confocal microscopy, we develop an approach to extend histological validation of orientation functions to 3D. We also describe appropriate alignment and orientation of the histological data to MRI data. The intention of this work is not a comprehensive validation of the strengths and weaknesses of the various dMRI algorithms, nor determination of optimal acquisition parameters. Rather, the focus is on the technique itself, which represents an advance in the development of a “gold standard” for the purposes of validating fiber orientation information. We begin with an in-depth description of the method, which employs a common image processing technique — structure tensor analysis — in order to extract the 3D FOD in areas equivalent in size to an MRI voxel. Next, we describe the sensitivity of this approach to confocal acquisition and image processing parameters. Finally, we apply this technique to both single fiber and crossing fiber white matter (WM) regions, and, as a methodological benchmark, make quantitative comparisons of the histological-FOD to the corresponding MRI-FOD derived using constrained spherical deconvolution (CSD) with the damped Richardson–Lucy algorithm (Dell’acqua et al., 2010).

## Materials and methods

### MRI acquisition

All animal procedures were approved by the Vanderbilt University Animal Care and Use Committee. Diffusion MRI experiments were performed on an adult squirrel monkey brain that had been perfusion fixed with physiological saline followed by 4% paraformaldehyde. Prior to fixation, the brain had undergone micro-electrode array recording experiments for an unrelated study. Due to this, there was slight atrophy in one hemisphere near the motor and pre-motor areas, resulting in asymmetric hemispheres in both histology and MRI. However, this does not impact the results of our study, which is focused on characterizing white matter structure by determining the underlying fiber orientation distribution. The brain was then immersed in 4% paraformaldehyde for 3 weeks. The brain was transferred into a phosphate-buffered saline medium for 24 h and scanned on a Varian 9.4 T, 21 cm bore magnet using a multi-shot multi-slice spin echo EPI sequence (TR = 6.7 s; TE = 42 ms;  $\delta$  = 8 ms;  $\Delta$  = 27 ms; max gradient strength = 30 g/cm; voxel size = 400  $\mu\text{m}$  isotropic; partial Fourier = .75; NEX = 5).

A 30-direction diffusion-sampling scheme based on an electrostatic repulsion algorithm (Jones et al., 1999) was used to acquire 30 diffusion-weighted images at a b-value of 3200  $\text{s/mm}^2$ , and 2 additional images were collected with  $b = 0$ . This set of data was used for calculating diffusion tensors using a weighted linear least squares fit. Next, a 90-direction scheme was used to acquire diffusion weighted-images at a b-value of 6400  $\text{s/mm}^2$ , and 6 additional images at  $b = 0$ . From this dataset, the MRI-FOD was estimated using constrained spherical deconvolution with the damped Richardson–Lucy algorithm (Dell’acqua et al., 2010) and fit to 8th order spherical harmonic (SH) coefficients. MRI data processing was done using the high angular resolution diffusion imaging (HARDI) toolbox for MATLAB, available at [http://neuroimaging.es/webs/hardi\\_tools/](http://neuroimaging.es/webs/hardi_tools/).

### Histological procedures

After imaging, the brain was sectioned on a cryomicrotome at a thickness of 80  $\mu\text{m}$  in the coronal plane and mounted on glass slides. Using a Canon EOS20D (Lake Success, NY, USA) digital camera with a zoom lens of 70–300 mm, the tissue block was digitally photographed prior to cutting every other section, resulting in a 3D “block-face” volume with a through-plane resolution of 160  $\mu\text{m}$ .

The tissue sections were mounted on glass slides and stained following the procedures outlined in (Budde and Frank, 2012). Briefly, tissue sections were rinsed in PBS and dehydrated through graded ethanol solutions. The fluorescent lipophilic dye, “DiI”, (1,1'-dioctadecyl-3,3,3'3'-tetramethylindocarbocyanine perchlorate) in 100% ethanol (.25 mg/mL) was rinsed over sections for 1 min. The stained sections were then rehydrated through graded ethanol solutions, and cover-slipped with Fluoromount-G mounting medium.

### Confocal acquisition

All histological data were collected using an LSM 710 inverted confocal microscope (Carl Zeiss, Inc. Thornwood, NY, USA). For all selected tissue slices, confocal acquisition consists of two protocols: [1] creating a 2D montage of the entire tissue and [2] constructing a 3D high-resolution image in a selected region of interest. The 2D montage (Fig. 1A) consists of approximately 600–900 individual tiles acquired using a 10 $\times$  air objective at a resolution of 0.80  $\mu\text{m}^2$ , which are stitched together using Zeiss software, ZEN 2010. Acquisition for a single slice takes approximately 30 min. To correct for image inhomogeneity and tiling effects in the image, we found it useful to increase the zoom feature to 1.5 $\times$  or higher at the expense of collecting more tiles. This 2D montage is used for image registration, and for localizing the 3D high-resolution region of interest.

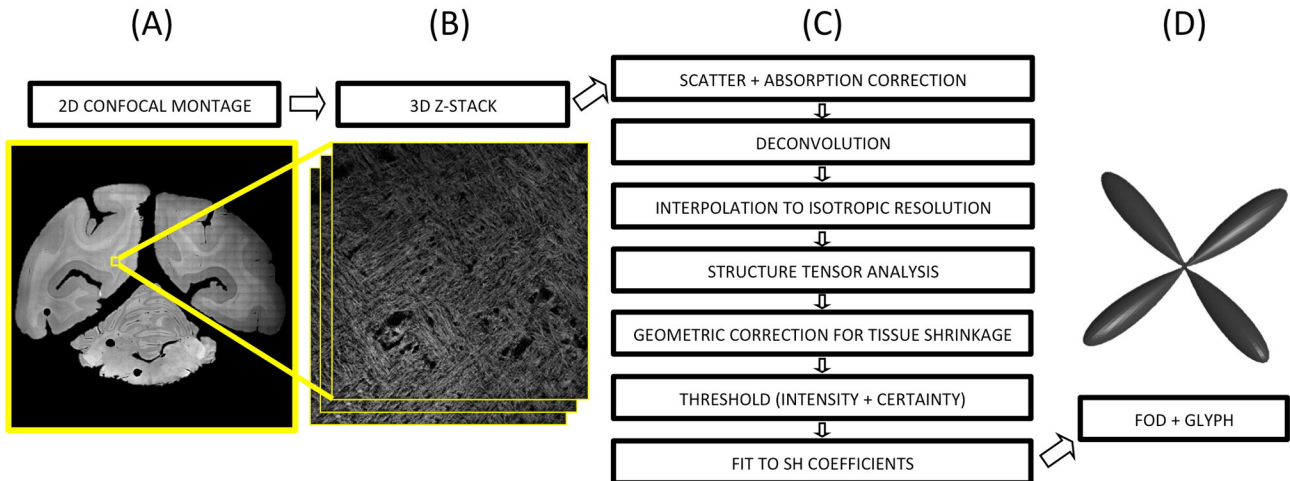


**Fig. 1.** Estimating the fiber orientation distribution from confocal z-stacks. Confocal acquisition includes a 2D low-resolution montage (A) and a high-resolution 3D z-stack (B). Image pre-processing (C) comprises light scatter and absorption correction, deconvolution, and interpolation. Next, structure tensor analysis is performed (illustrated in Fig. 2 on a simulated fiber), and the tertiary eigenvector extracted for all pixels. This is followed by geometric correction for tissue shrinkage, thresholding fibers, and fitting to spherical harmonic coefficients. The resulting FOD is displayed as a 3D glyph (D).

Prior to 3D z-stack acquisition, two steps are performed. First, tissue thickness in the z-dimension is determined by adjusting the focal plane depth to determine where fluorescence begins and ends. This thickness is used to correct orientation estimates for tissue shrinkage (see **Histological FOD** below). Second, it is necessary to increase the laser output as deeper layers are imaged due to the increases in light scatter and absorption at greater tissue depths (see **Confocal pre-processing**). The laser power is adjusted for approximately 5 different depths ranging from the coverslip to the end of the tissue, at each step ensuring that the image intensity range will cover the full 8-bit depth from 0 to 255 units. The LSM 710 interpolates the laser output between depths.

The 3D z-stack (Fig. 1B) is then collected using a  $63 \times$  oil objective at a nominal resolution of  $0.18 \mu\text{m} \times 0.18 \mu\text{m} \times 0.42 \mu\text{m}$ . Typical acquisition time to acquire the entire section thickness with an in-plane field of view of  $1.6 \text{ mm} \times 1.6 \text{ mm}$  (equivalent to 16 MRI voxels) is approximately 8 h. The through-plane resolution is the “optimal” slice-thickness, calculated from the LSM710 software based on a 1.0 Airy unit pinhole diameter and an excitation wavelength of 543 nm. Stitching, again, is performed using ZEN 2010 software to create a single 3D z-stack.

Finally, all confocal data are converted from the LSM file format to TIFF images and imported into MATLAB for further processing.

#### Confocal pre-processing

The aim here is to extract the histological-FODs from the 3D z-stacks in areas equivalent to the size of an MR voxel. To do this, we use structure tensor analysis to obtain an orientation estimate for every pixel in the 3D z-stack that is occupied by a fiber.

Prior to structure tensor analysis, four sources of anisotropy inherent to confocal microscopy must be accounted for (Fig. 1C). Three corrections are performed directly on the confocal z-stack prior to structure tensor analysis, and the final correction performed post-analysis. The first is an attenuation of the image intensity as a function of tissue depth. This effect is caused by light scatter and absorption which decreases the intensity of excitation light penetrating to the deeper layers of the tissue, and consequently, the fluorescence of these layers. Because structure tensor analysis is based on image intensity gradients, this artifact could result in a bias in fiber orientation estimates (Khan et al., 2015). The attenuation correction is performed in the **Confocal acquisition** stage described above. Increasing the laser power for deeper

layers generates a z-profile that has a relatively constant mean intensity in each x-y plane containing fibers.

The second source of anisotropy arises from the confocal microscope's point spread function (PSF). The PSF is the 3D diffraction pattern resulting from the system's response to an infinitely small point source of light. This diffraction pattern is known to be nearly three times wider through-plane than in-plane (Pawley and Masters, 1996), leading to anisotropic blurring of the image; in-plane structures will be better resolved than those oriented through-plane. To deblur the confocal data, we use the iterative Lucy–Richardson algorithm (Biggs and Andrews, 1997) and a computed theoretical model of the confocal microscope's PSF (Pawley and Masters, 1996). This model takes into account various confocal parameters including the numerical aperture, refractive index, wavelength of light, and the acquired image resolution. The Lucy–Richardson deconvolution algorithm is a maximum-likelihood approach to find the statistically most likely image, given the blurred image and assuming Poisson noise (Biggs, 2010; Biggs and Andrews, 1997), which is an appropriate noise model of the photon-counting process of confocal imaging (Pawley and Masters, 1996).

The final pre-processing step is to correct for the anisotropic acquisition resolution. This ensures that fibers oriented laterally in the image will contain an equivalent number of pixels per length as fibers oriented axially. Interpolation to isotropic resolution is accomplished using cubic interpolation.

#### Structure tensor analysis

The structure tensor was introduced in the late 1980's for point and edge detection (Bigun and Granlund, 1987; Harris and Stephens, 1988), and has since become popular in image processing and computer vision, with applications including texture analysis and materials science (Axelsson, 2008; Krause et al., 2010). This analysis technique is applied to our entire 3D confocal image,  $f(x,y,z)$ . The structure tensor (Köthe, 2003) is based on the gradient of  $f$ :

$$\nabla f_\sigma = (f_x, f_y, f_z)^T \quad (1)$$

which is calculated with Gaussian derivative filters:

$$f_x = g_{x,\sigma} * f, \quad f_y = g_{y,\sigma} * f, \quad f_z = g_{z,\sigma} * f \quad (2)$$

where  $*$  denotes the convolution operation and  $g_{x,\sigma}$ ,  $g_{y,\sigma}$ , and  $g_{z,\sigma}$  are the spatial derivatives in the  $x$ ,  $y$ , and  $z$ -directions, respectively, of a 3D Gaussian with standard deviation  $\sigma$ :

$$g_\sigma(x, y, z) = \frac{1}{(\sqrt{2\pi\sigma^2})^3} e^{-\frac{(x^2+y^2+z^2)}{2\sigma^2}} \quad (3)$$

For illustration purposes, we show this step as performed on a simulated cylindrical fiber (Fig. 2A), representative of the neuronal structures seen in the 3D confocal image (similar illustrations appear in (Khan et al., 2015) and (Arseneau, 2006)). Ideally, the image gradients are orthogonal to the fibers at all points (Fig. 2B). Next, an object known as the gradient square tensor, is calculated for each point in the image by taking the dyadic product of the gradient vector with itself:

$$GST(x, y, z)_\sigma = \nabla f_\sigma \nabla f_\sigma^T = \begin{pmatrix} f_x^2 & f_x f_y & f_x f_z \\ f_x f_y & f_y^2 & f_y f_z \\ f_x f_z & f_y f_z & f_z^2 \end{pmatrix} \quad (4)$$

Each tensor element is averaged over a local neighborhood to create the pixel-wise structure tensor. For spatial averaging, we choose a 3D Gaussian filter with standard deviation  $\rho$ :

$$ST_\rho(\nabla f_\sigma) = g_\rho * (\nabla f_\sigma \nabla f_\sigma^T) \quad (5)$$

This results in a 3-by-3 symmetric, semi-positive definite, rank-two tensor. Much like the diffusion tensor, this matrix will have three positive eigenvalues, and can be visualized as an ellipsoid (Fig. 2C). In DTI, one is typically interested in the largest eigenvalue and eigenvector, which points in the direction of greatest diffusion, and is usually assumed to be parallel to the primary structure orientation in the MR voxel. However, in structure tensor analysis, the image intensity gradients are strongest perpendicular to the fibers, which means the largest

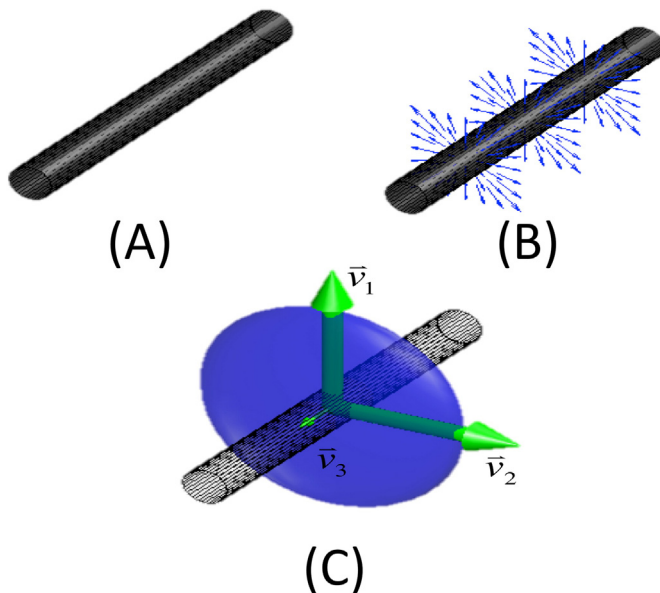


**Fig. 2.** Structure tensor analysis illustrated on a simulated cylindrical fiber (A). The structure tensor is derived from the image intensity gradients (B), which point orthogonal to the fiber at all points. The Cartesian product of the gradient vector with itself is taken, and averaged over a local neighborhood to derive the structure tensor, which has 3 eigenvalues and 3 eigenvectors (C). The tertiary eigenvector,  $v_3$ , will point in the direction of minimum intensity variation – parallel to the fiber.

two eigenvectors will also be perpendicular to the fiber bundles. Hence, we make the assumption that the direction of minimal intensity variation is parallel to the fiber orientation at each pixel, a direction given by the eigenvector corresponding to the smallest eigenvalue.

The certainty in estimated fiber orientation can be described by the Westin-measure (Westin et al., 2002) defining how planar the structure tensor is:

$$c_p = \frac{\lambda_2 - \lambda_3}{\lambda_1} \quad (6)$$

where  $\lambda_1$ ,  $\lambda_2$ , and  $\lambda_3$  are the primary, secondary, and tertiary eigenvalues of the structure tensor. This value varies from 0 to 1 and will be large in areas, like that depicted in Fig. 2C, where the first two eigenvalues are much larger than the third. This measurement is used to threshold the confocal image, so voxels with low certainties are not included in the final orientation distribution.

For the results presented in this paper, the spatial derivatives were calculated using a Gaussian with standard deviation  $\sigma = 1 \mu\text{m}$ , and spatial averaging performed using a Gaussian with standard deviation  $\rho = 2.5 \mu\text{m}$  (these values were chosen based on comparisons to distributions of manually traced fibers – see [Sensitivity analysis](#)).

#### Histological-FOD

After a fiber orientation has been extracted for all pixels in the image (Fig. 1C) one final correction for anisotropy must be performed. It is known that tissue samples may shrink due to processing, sectioning, and staining (Eltoum et al., 2001; Woods AE, 1994). These effects are mainly a result of fixation and dehydration in alcohol solutions during the staining procedure (Wehrle et al., 2015; Williams et al., 1997). We use the thickness measurement before acquisition of each 3D z-stack to perform a geometric correction to the orientation estimate for every pixel in the image by assuming linear shrinkage in the through-plane ( $z$ ) direction.

Once all estimated vectors have been appropriately re-oriented to account for tissue shrinkage, the results are thresholded using both image intensity and the certainty value. This yields an orientation estimate for every pixel in our z-stack that is occupied by a fiber.

A histogram representing the histological-FOD is then created as a function of polar and azimuthal angle, where the orientation estimates are placed into bins that cover constant solid angles over a sphere. This FOD is fit to high order (20) SH coefficients, and throughout this paper is displayed as a three dimensional glyph (Fig. 1D) in the same way that the MRI-FOD's are typically displayed.

#### Image registration

In order to make a quantitative comparison of the histological-FOD and the MRI-FOD, the data must be aligned and oriented appropriately. A multi-step registration procedure (Choe et al., 2011) was used to align histology to MRI data. The first step is registration of the 2D confocal montage to the corresponding block face image using mutual information based 2D linear registration followed by 2D nonlinear registration using the adaptive bases algorithm (ABA) (Rohde et al., 2003). Next, all block face photographs were assembled into a 3D block volume, which is registered to the MRI  $b = 0$  image using a 3D affine transformation followed by 3D nonlinear registration with ABA. Given the location of the 3D z-stack in the 2D confocal montage, we can use the combined deformation fields to determine the MRI signal from the same tissue volume. The MRI signal of interest is analyzed in MRI native space. As described above, we derive the tensor using a WLLS fit, and estimate the MRI-FOD using constrained spherical deconvolution.

The final step is to transform the diffusion tensor and MRI-FOD to histological space to facilitate comparisons with the histological FOD. For the tensor, we apply the preservation of principal directions (PPD)

strategy (Alexander et al., 2001) twice: once to transform the tensor from MRI-space to block-space, and again to transform to histological space. For the MRI-FOD, we choose the approach developed in Hong et al. (Hong et al., 2009). This method takes into account rotation, scaling, and shearing effects of the spatial transformations, and can be applied to any orientation distribution on a sphere. After these corrections, both the histological-FOD and the MRI-FOD are in histological space, and quantitative analysis can be performed.

## Results

### Sensitivity analysis

We begin by reporting the sensitivity of this technique to acquisition and image analysis parameters. First, three single fiber regions (with three different primary orientations) were acquired at in-plane resolutions ranging from  $0.08 \mu\text{m} \times 0.08 \mu\text{m}$  to  $0.42 \mu\text{m} \times 0.42 \mu\text{m}$ . The through-plane resolution was set to  $0.42 \mu\text{m}$  for all sets. Structure tensor analysis was performed on all datasets with parameters  $\sigma = 1 \mu\text{m}$  and  $\rho = 2.5 \mu\text{m}$ . To determine the ground truth fiber distribution, 100 fibers (seeded from 100 random voxels) were manually traced in the highest resolution dataset, the corresponding histogram fit to spherical harmonic coefficients, and the primary orientation extracted as performed above. The angular error between the ground truth orientation and the results from structure tensor analysis is shown in Fig. 3 (left). It is clear that higher resolution provides the most accurate representation of fiber direction, however, even isotropic resolution had an average error of less than  $5.0^\circ$ .

Next, the sensitivity of the analysis to the standard deviation of the first derivative Gaussian,  $\sigma$ , was analyzed. This was done using the z-stacks acquired at  $0.18 \mu\text{m} \times 0.18 \mu\text{m} \times 0.42 \mu\text{m}$ ,  $\rho = 2.5 \mu\text{m}$ , and a range of  $\sigma$  (Fig. 3, middle). We find a range of kernel sizes, with  $\sigma$  between  $0.5 \mu\text{m}$  and  $2 \mu\text{m}$  that result in accurate orientation results. This optimal range closely matches the size of the myelinated fibers in the image, which we found to have diameters in the range of  $0.5 \mu\text{m}$ – $1.5 \mu\text{m}$ . Outside this range, the results become unreliable. In particular, too large a kernel will result in a significant blurring of the image, which leads to large areas of isotropic intensity, and an almost random orientation estimate for all pixels. The error begins to approach the expected value for the angle between two randomly oriented lines through the origin, 1 rad or  $57.3^\circ$  (Cai et al., 2013).

Finally, we find that the method is relatively robust to the averaging kernel size,  $\rho$  (Fig. 3, right). With a resolution of  $0.18 \mu\text{m} \times 0.18 \mu\text{m} \times 0.42 \mu\text{m}$  and  $\sigma = 1 \mu\text{m}$ , all values of the averaging kernel gave an estimate of the primary fiber direction accurate to within  $4^\circ$ .

### Image registration

An example of the correspondence between histology and MRI after registration is shown in Fig. 4. The top row shows the 2D confocal montage (A1), the corresponding block-face image (A2), and the MRI data (A3), all aligned in the intermediate “block-space”. These whole-slice images show agreement of large-scale features, including sulci and gyri, and major white matter tracts. A magnified region of interest is also shown for each modality (A4–A6). The asterisk indicates the location of the center of the 3D confocal z-stack acquired and displayed in Fig. 9E. The arrows highlight anatomical landmarks and are drawn at the same position on each image. It is clear that smaller scale features still share precise shape, position and alignment on all three modalities.

Similarly, panels (B1–B3) assess the registration accuracy from the slice corresponding to that shown in Fig. 9A. While not strictly necessary, we chose to manually remove the cerebellum from the confocal and block images to facilitate registration, as is commonly done in studies where this structure is of no interest (Dauguet et al., 2007; Singh et al., 2008). Again, we see excellent agreement between histology, block, and MRI on the scale of the full slice (B1–B3) and at the voxel-wise scale (B4–B6).

### Single fiber analysis

The results of 3D structure tensor analysis in regions of the brain containing predominantly single fiber populations are shown in Fig. 5 (rows 1 and 2). Structure tensor analysis demonstrates the corpus callosum (Fig. 5A) is composed of fibers running in the right–left orientation and remaining largely in-plane. Visually, this corresponds well with the primary fiber orientation derived from MRI, including the CSD-FOD (row 3) as well as the apparent diffusion coefficient profile of the diffusion tensor (row 4), calculated as the negative log of the normalized diffusion signal. Histological results from the optic tract (Fig. 5B) and external capsule (Fig. 5C) demonstrate the ability of this technique to describe obliquely-oriented, or slightly through-plane, fibers as well as those oriented completely through-plane, respectively. Again, the 3D structure tensor results qualitatively agree well with both the MRI-derived FOD and diffusion tensor.

Fig. 6 shows cloud plots of angular error in peak orientations between diffusion MRI and histology for 74 voxels in 10 different regions of the brain containing only a single fiber population. The average magnitude angular error (in 3D) was  $6.4^\circ \pm 4.0^\circ$  for CSD and a larger error of  $11.2^\circ \pm 5.9^\circ$  for DTI. For CSD, the mean in-plane orientation error was  $-0.8^\circ \pm 6.5^\circ$ , and through-plane was  $1.7^\circ \pm 4.0^\circ$ . The mean DTI error was  $-3.8^\circ \pm 6.5^\circ$  in-plane and  $-6.6^\circ \pm 7.9^\circ$  through-plane.

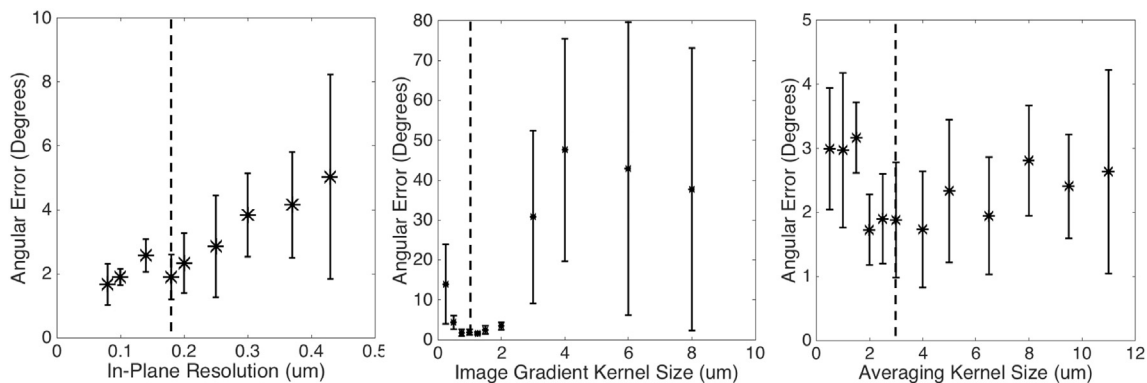


**Fig. 3.** Sensitivity of structure tensor analysis to imaging and image processing parameters. Ground truth fiber orientation distribution was determined for three confocal z-stacks by manually tracing 100 fibers per confocal volume. Angular error in the primary fiber orientation is plotted as a function of the in-plane confocal resolution (left), the standard deviation ( $\sigma$ ) of the Gaussian kernel used for calculating spatial derivatives (middle), and the standard deviation ( $\rho$ ) of the Gaussian kernel used for spatial averaging (right). Dashed lines indicate the parameters chosen for this study.

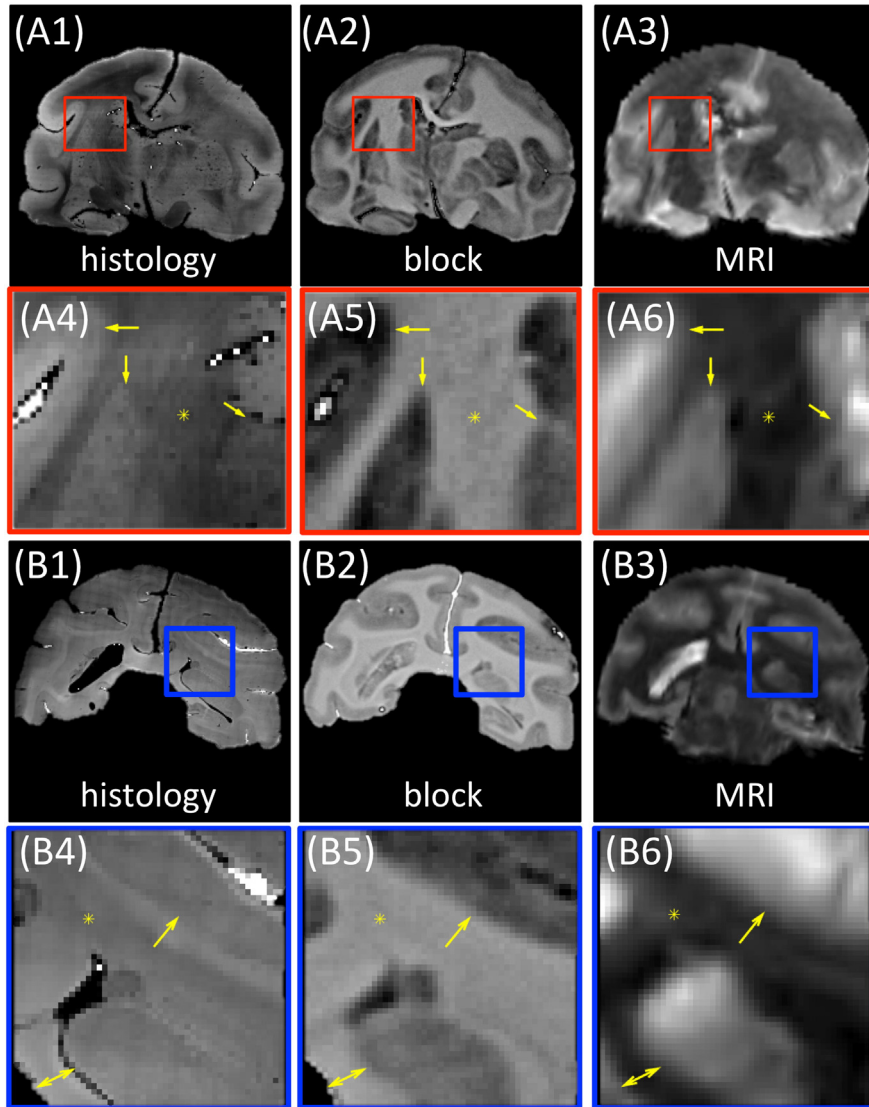


**Fig. 4.** Selected histological slices show the correspondence of matching between MRI and histology of the full slice and magnified views. The top two rows correspond to histological slice shown in Fig. 9E, and displays histology (A1), the matching block-face (A2) and the non-diffusion weighted MRI images (A3), all registered to the intermediate “block space”. The magnified views (A4–A6) show that MRI can be correlated on the voxel level to histology. The arrows highlight anatomical borders or edges between white and gray matter, while the asterisk indicates the location of the center of the acquired 3D z-stack. The lower two rows show the slice from Fig. 9A (note that the cerebellum was removed to facilitate registration). Again, there is a large scale agreement between histology (B1), block-face (B2), and the registered MRI (B3). Magnified views are displayed in figures (B4–B6) and show agreement on the voxel-wise scale. The asterisk, again, indicates the center of the 3D z-stack, while arrows facilitate comparisons by highlighting anatomical similarities.

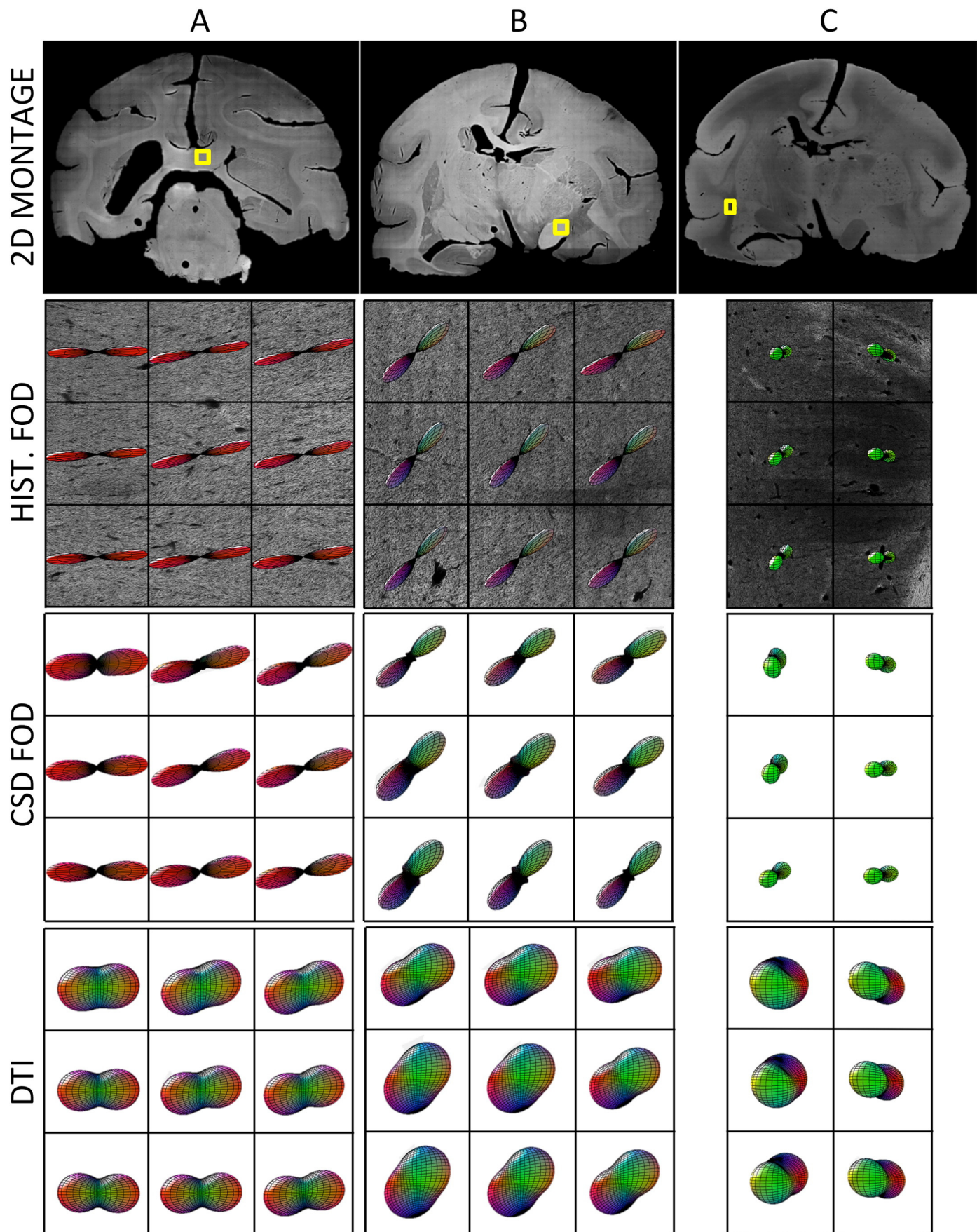
While the regions in Fig. 5 represent voxels containing classic single fiber populations, an in-depth examination of the histology depicts a “spread” of orientations in these imaging voxels. For example, structure tensor analysis of the corpus callosum voxel (Fig. 7A) shows an anisotropic fanning of the fibers while the optic tract voxel (Fig. 7B) shows axonal orientation dispersion symmetric around the predominant orientation. A common analysis approach in the literature is to fit these to a distribution on a sphere in order to extract parameters that can be used to describe geometric patterns (Ferizi et al., 2013). One such distribution is the Bingham distribution (Bingham, 1974), an antipodally symmetric distribution with elliptical contours on the sphere that is well suited for representing asymmetric or anisotropic dispersion

(Sotiroopoulos et al., 2012). If fit to the Bingham distribution, the voxel in the corpus callosum results in anisotropic concentration parameters:  $\kappa_1 = 21$ ,  $\kappa_2 = 12$ , confirming slightly anisotropic fanning geometry (fanning in the S/I direction). The optic tract voxel has slightly larger, but isotropic, dispersion:  $\kappa_1 = 10$ ,  $\kappa_2 = 9$ , consistent with a symmetric orientation dispersion.

#### Crossing fiber analysis

Fig. 8 demonstrates the advantages of using 3D acquisition and analysis over previous studies limited to 2D. The confocal montage (Fig. 8A) was used to choose a voxel for high-resolution acquisition that visually

**Fig. 5.** Qualitative single fiber analysis. Three large white matter tracts containing a single fiber population are shown, including the corpus callosum (A), optic tract (B), and external capsule (C). The 2D confocal montage of the tissue for each slice (row 1) highlights the locations of the 3D-confocal z-stack (yellow box). Histological FOD (row 2) is shown overlaid on a single slice of the z-stack. The MRI-FOD (row 3) and tensor (row 4) for corresponding voxels are displayed as 3D glyphs. All glyphs are color coded based on orientation, where red, green, and blue represent orientations in the left-right, superior-inferior, and anterior-posterior directions, respectively. Note that the third column from the external capsule (C) contained predominantly gray matter and has been excluded from analysis.



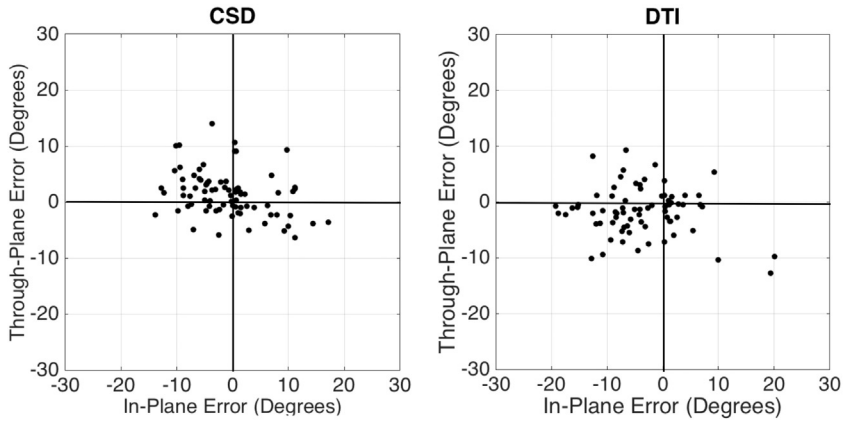


**Fig. 6.** Quantitative single fiber analysis. Cloud plots display angular error between MR and histology for CSD (left) and DTI (right) derived orientation estimates. Orientations are projected onto the xy-axis (in-plane) and the yz-axis (through-plane).

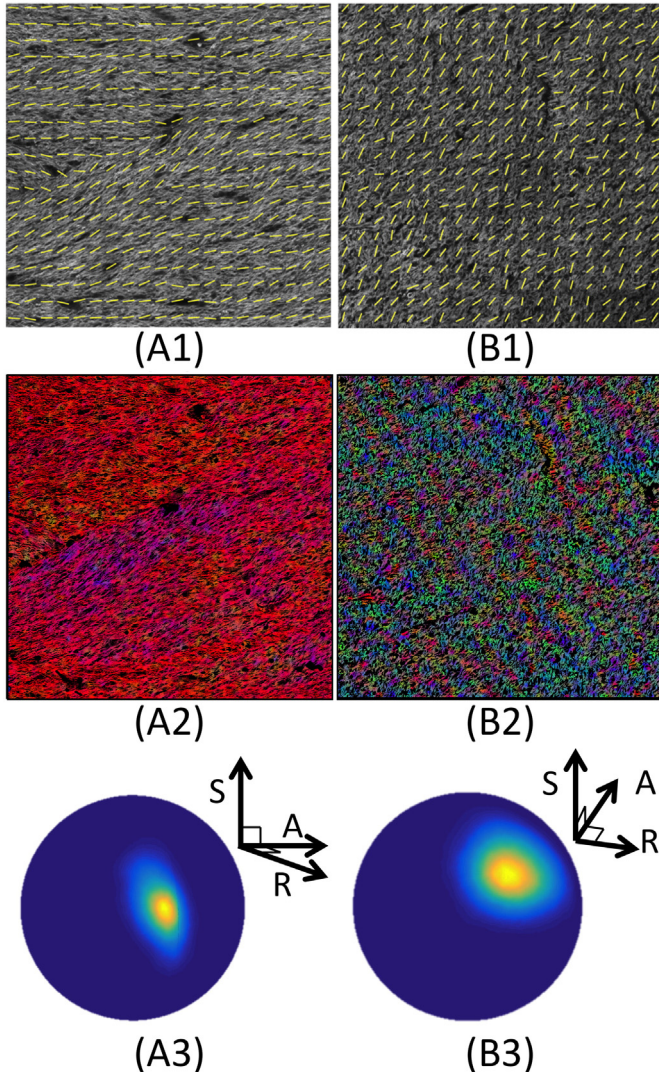


**Fig. 7.** Orientation dispersion in single fiber regions. Vector maps (A1, B1) display fiber orientation projected onto xy plane. In colormaps (A2, B2) fibers are orientationally color-coded using the coloring scheme described in Fig. 5. The FOD is further displayed as a distribution over the unit sphere (A3, B3). These have been rotated to better visualize the dispersion patterns. The voxel from the corpus callosum (A) is the center voxel depicted in Fig. 5A, while that from the optic tract (B) is also the center voxel from Fig. 5B. Note that both voxels display a spread of orientations.

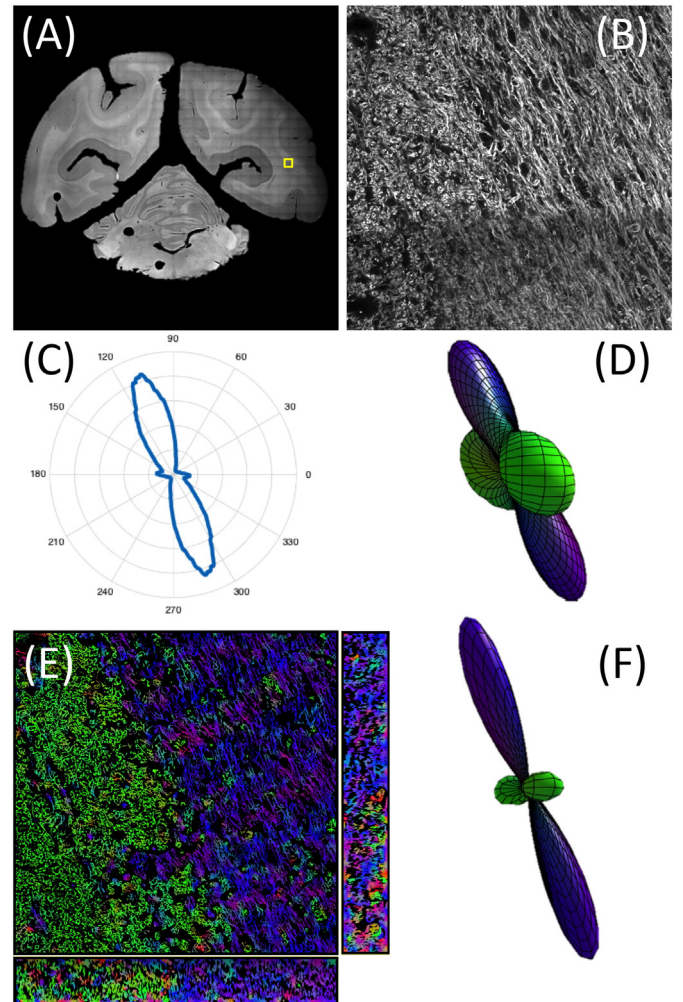


**Fig. 8.** Crossing fiber analysis in 2D and 3D. The 2D confocal montage (A) highlights the location of the high-resolution 3D z-stack (B). 2D structure tensor analysis was performed on a single slice and the results shown in the 2D rose plot (C) suggest a single fiber population, while CSD-MRI data (D) suggest two fiber populations. Results from 3D structure tensor analysis are displayed as a colormap of the slice (E), along with the two orthogonal views, using the color scheme described in Fig. 2, as well as FOD glyph (F), both of which highlight the fact that two distinct fiber orientations are present.

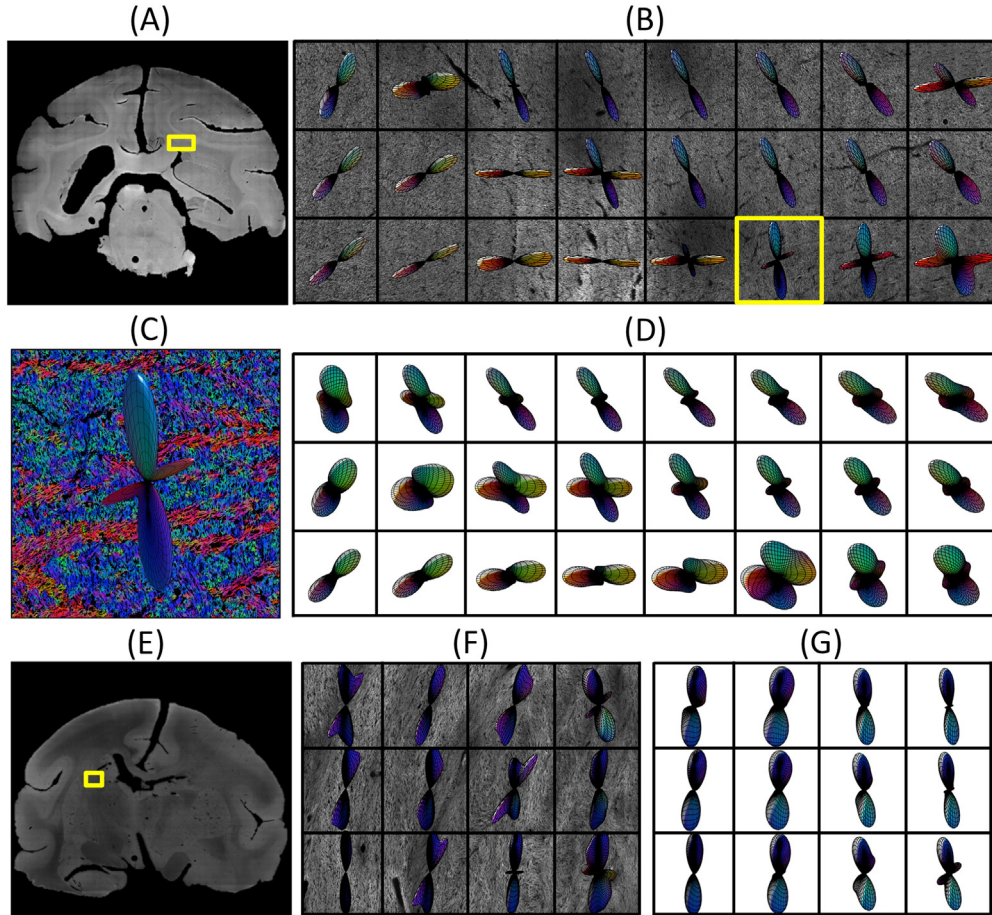
appeared to contain fibers oriented both in-plane and through-plane (Fig. 8B). The middle slice of the z-stack was chosen for conventional 2D analysis using the methods described in Budde and Frank (2012). These results (Fig. 8C) suggest a single fiber population in this voxel, oriented primarily in the superior–inferior direction. However, the MR data indicate the presence of multiple fibers (Fig. 8D), which is verified with 3D structure tensor analysis, shown as a color-coded fiber map (Fig. 8E) and 3D glyph (Fig. 8F).

Fig. 9 further demonstrates the ability of 3D structure tensor analysis to capture the crossing of fiber bundles in 3D. A  $3.2\text{ mm} \times 1.2\text{ mm}$  region where the corpus callosum meets the corona radiata is highlighted (Fig. 9A) along with the structure tensor results from the histological z-stack (Fig. 9B), where the two dominant fiber bundles and their intersection are readily apparent. These results qualitatively agree with the FODs derived from MRI data (Fig. 9D).

The ability to extract orientation information from complicated crossing geometries is highlighted in Fig. 9C, where fibers running right to left (Fig. 9C, red) interdigitate with the majority of fibers which run superior to inferior (Fig. 9C, blue). Further, regions with very sharp crossing angles can be identified (Fig. 9E) and resolved with structure tensor analysis (Fig. 9F). The dominant orientations again agree well with those from CSD (Fig. 9G), however, regions with multiple crossings at acute angles are often not identified in MRI as having multiple fiber populations.

Forty histological voxels were identified through structure tensor analysis as having multiple fiber populations, and quantitatively compared to CSD results. The algorithm to determine whether a voxel contains crossing fibers is described in (Jansons and Alexander, 2003).

Briefly, the histological FOD is sampled in a large number of evenly distributed directions on a unit sphere and local maxima identified (local maxima are defined to be greater than any other samples within a search radius of  $0.25\text{ rad}$ ). Similarly, the FOD's of the corresponding MRI-CSD results were analyzed. In order to remove spurious peaks, those with amplitude less than 10% of the amplitude of the largest peak, as well as peaks that did not correspond with any histological peak to within an angular error of  $30^\circ$ , were discarded. The results of this analysis are shown in Fig. 10. The average magnitude angular error was  $10.4^\circ \pm 5.1^\circ$  for the primary (largest amplitude) fiber orientation (Fig. 10, left), and  $11.6^\circ \pm 7.0^\circ$  for the secondary orientation (Fig. 10, right), both of which are larger than the error associated with single fiber regions. For the primary direction, the mean in-plane orientation error was  $-0.1^\circ \pm 9.7^\circ$ , and through-plane was  $3.5^\circ \pm 5.7^\circ$ , while that for the secondary direction was  $-0.2^\circ \pm 10.4^\circ$  and  $3.6^\circ \pm 8.4^\circ$ , respectively. Finally, we employ a commonly used measure, the success rate, as a function of fiber crossing angle (Fig. 10). The success rate measures the proportion of voxels containing two fiber orientations (as identified by histology) where two peaks could also be identified by the chosen MRI algorithm. From the 40 identified voxels with multiple fiber populations, only 29 of the corresponding MRI voxels exhibited the presence of crossing fibers after spherical deconvolution. With this dataset, CSD consistently failed (<20% success rate) to resolve crossing fibers in regions where histology identified crossing at angles below  $60^\circ$ , while the success rate was high for fibers crossing at angles above  $70^\circ$ . Further, DTI failed to resolve crossing at all angles, which was expected (Wiegell et al., 2000), as the tensor model represents only one dominant direction.



**Fig. 9.** Qualitative crossing fiber analysis. The intersection of the corpus callosum and corona radiata (A) was imaged in 3D, and FOD's from structure tensor analysis are displayed (B). The yellow box highlights the voxel displayed in (C) where interdigitating fibers running right–left are visible in both the colormap and the 3D glyph. The MRI results using CSD (D) appear to be a blurred version of the histological FOD, where primary orientations largely agree. The region identified in (E) is shown to contain fanning structures and bundles crossing at sharp angles (F), while the MRI data (G) fail to resolve sharp crossing angles.

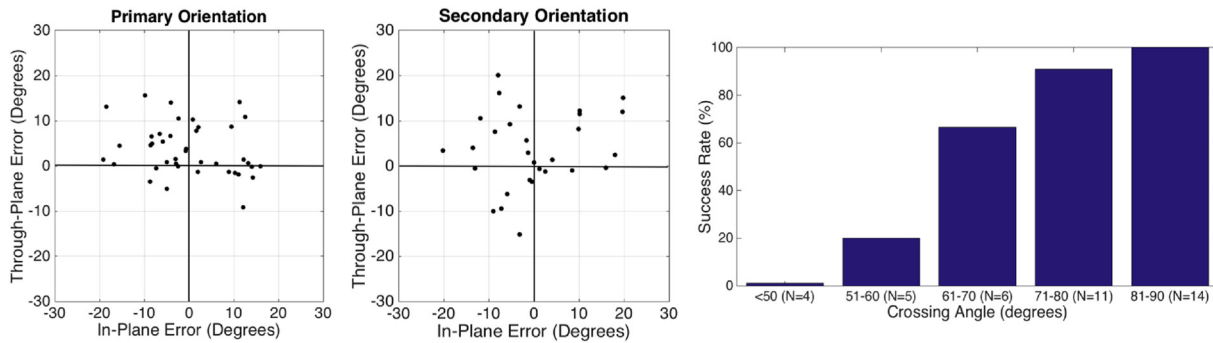


**Fig. 10.** Quantitative crossing fiber analysis. Cloud plots display angular error between MR and histology for the primary fiber orientation (left) and secondary fiber orientation (middle) in regions with crossing fibers. Orientations are projected onto the xy-axis (in-plane) and the yz-axis (through-plane). The success rate of CSD with the damped Richardson–Lucy algorithm is reported as a function of fiber crossing angle as identified by histology (right). The sample size is also noted for each crossing angle bin.

## Discussion

Diffusion MRI-based non-invasive mapping of the three-dimensional network of connections in the brain has gained widespread use in the neuroimaging community. These tractographic reconstructions result in exquisite images of the human brain that can easily be over-interpreted or misinterpreted. Thus, validating diffusion imaging's ability to assess the underlying fiber orientation in each voxel is critical for its use as a biomedical tool.

The use of ex vivo histology as a “gold standard” holds promise, as it provides true axonal characteristics at the micron and voxel-sized scales, including microstructural compartments, biophysical properties, and complex tissue geometries. This work presents an extension of histological validation of orientation functions to three dimensions. Previous orientation validation studies have been limited in that they required identification of suitable regions of interest where 3D FODs could be compared to the inherently 2D coronally sectioned histological data. This also necessitated sectioning the tissue block orthogonal to the primary directions of interest for adequate analysis, as any through plane fibers would be undetected (Budde and Frank, 2012) and could lead to misleading orientation results (Fig. 8C). While the use of 3D optical imaging to validate dMRI has recently gained traction, determination of the white matter histological fiber orientation distribution has not yet been reported. For example, the current study shares many methodological similarities with Khan et al., 2015, including structure tensor analysis of confocal data (see Data pre-processing). However, rather than assessing the orientation of all individual axons, the focus in that study was on quantitative comparisons of dMRI and structure tensor measures (FA, eigenvalues) on the scale of 10's–100  $\mu\text{m}$ . Similarly, Jespersen et al., 2012, performed a 3D analysis of Golgi-stained tissue, but with aim of deriving the dendritic and axonal orientations in the cerebral cortex.

The use of histology for validation studies presents several potential limitations. Two of these are the data registration problem, and the imaging depth limitation inherent to confocal microscopy. Mapping high resolution histological data onto the MRI images is known to be a challenge because of the many differences between the histological slices and the original brain tissue (Dauguet et al., 2007). The process of fixation and brain extraction can lead to mechanical distortions in the tissue, while cutting, placing slices on slides, and staining can cause contractions, non-linear distortions, and separation of the hemispheres (Dauguet et al., 2007). In this study, these problems are addressed through the use of linear and non-linear registration of the datasets. For data alignment, the acquisition of the block-face image data is crucial; it provides an undistorted 3D image of the brain before sectioning, and operates as an intermediate step in registration of the potentially distorted histology to the MR data (Toga et al., 1994). Previously, this technique has been shown to provide registration accurate to approximately the size of the MRI

voxel (Choe et al., 2011). Tissue contraction (shrinkage) is further accounted for in the confocal pre-processing steps (and discussed in Data pre-processing). The imaging depth limitation of confocal microscopy is also discussed in Data pre-processing.

### Single fiber analysis

The peaks of the histological FOD correspond well with those obtained with DTI and CSD in regions containing predominantly a single fiber population. While DTI had a larger angular error than CSD reconstruction (11.2° versus 6.4°, respectively), this is potentially a result of differing acquisition protocols (lower b-value and fewer sampling directions for DTI) rather than DTI being an inferior technique in single fiber regions. These mean angular errors are slightly larger than simulation (Jones, 2004) and phantom (Yanasak and Allison, 2006) studies with similar imaging conditions, emphasizing the importance of incorporating the complex tissue geometries seen in vivo. Further, the in-plane orientation errors agree well with previous 2D histological validation studies (Choe et al., 2012; Leergaard et al., 2010), which were only able to capture in-plane orientation estimates. These results verify that confocal analysis and image processing are able to extract fiber orientation distributions in 3 dimensions from histological data, thus serving as a methodological benchmark.

A closer look at these regions shows that the underlying geometry may be more complex than an idealized single fiber bundle where all fibers are assumed to be running parallel within the voxel. For example, histology (Fig. 7) depicts a spread of orientations in the form of fiber-fanning, or in wave-like undulations. Recently, there has been interest in characterizing this spread by using dispersion indices in order to infer the underlying fiber geometry (Nilsson et al., 2012; Tariq et al., 2014; Zhang et al., 2012). While the CSD and DTI methods implemented assume axially symmetric profiles, 3D structure tensor analysis is well suited for studying the axonal angular dispersion, even in highly organized white matter tracts. Thus, the methods presented in this study can provide a valuable resource in validation of this challenging inverse problem.

### Crossing fibers

Understanding the limitations of dMRI in crossing fiber regions is an active area of research. Here, we chose to analyze our data using a spherical deconvolution model, which aims to reconstruct the FOD directly. However, there are a variety of high angular resolution approaches to reconstruct orientation estimates that could be validated against histology, including, but not limited to, Q-ball Imaging (Tuch, 2004), DSI (Wedeen et al., 2005), multi-tensor (Tuch et al., 2002) or ball-and-stick models (Behrens et al., 2003), persistent angular structure models (Jansons and Alexander, 2003), diffusion orientation transform (Ozarslan et al., 2006), and the CHARMED model (Assaf and

Basser, 2005). While this study does not present a full validation, it is important to point out that with the current imaging parameters (SNR ~15, sampling directions = 90, b-value = 6400 s/mm<sup>2</sup>, roughly equivalent attenuation profile as an *in vivo* value of ~2000 s/mm<sup>2</sup>), CSD was not able to consistently resolve fibers crossing at angles below 60°. This is in close agreement with simulations performed by (Daducci et al., 2014) which found a success rate of approximately 20% for constrained spherical deconvolution (Tournier et al., 2007) at crossing angles below 60° with an SNR of 30, b-value of 3000 s/mm<sup>2</sup>, and 60 sampled directions. Additionally, simulating crossing fibers with equal fiber volume fractions, an SNR of 30, and a b-value of 1000 s/mm<sup>2</sup> (Descoteaux et al., 2009) find an angular resolution limit using CSD of 54°.

It is important to emphasize that we do not want to draw broader conclusions regarding this reconstruction method without larger sample sizes and an optimized acquisition protocol that would be appropriate to validate this (and other) models and parameters. Thus, future work will determine the relationship between the MRI signal and the histological FOD as a function of diffusion model, b-value, number of diffusion encoding directions, SNR, and scan time equivalence. Validation using structure tensor analysis is not limited to CSD methods, and can easily be applied to any of the existing techniques for modeling orientation functions in order to test the limitations of these techniques or to determine optimal acquisition parameters.

#### Sensitivity

**Fig. 3** shows that 3D structure tensor analysis is relatively robust to the resolution of the confocal z-stack. The angular error closely follows intuition – the higher the image resolution, the more accurate are the orientation measurements. The final choice of in-plane resolution, 0.18 μm × 0.18 μm, was a compromise between orientation accuracy and scan time. A more than two-fold reduction in resolution from 0.08 μm<sup>2</sup> to 0.18 μm<sup>2</sup> leads to a minimal loss of accuracy, yet allows acquisition of a field of view greater than 4 times larger in a given scan time.

We found our technique is quite sensitive to the kernel used for calculating spatial derivatives. While this step can be performed using a simple finite difference kernel (e.g. forward, backward, central difference) along all three axes, a Gaussian derivative is most commonly used as a regularization step to improve SNR and decrease sensitivity to noise. This also makes the algorithm sensitive to structures that correspond to the size of the Gaussian derivative. This explains the lower angular error when the kernel size is approximately the size of the myelinated fibers, which are the objects we wish to detect in the image.

Finally, the structure tensor analysis was not particularly sensitive to the averaging kernel size. This kernel serves to combine all orientation information in a local neighborhood, which leads to better estimates and reduced local errors in orientation estimates. Any low-pass filter can accomplish this smoothing operation, however, if two distinct orientations exist in a neighborhood, an averaging operation could lead to erroneous estimates. Thus, we chose an averaging kernel large enough to encompass the surfaces normal to the fiber, but small enough to resolve fibers interdigitating on scales as small as 2.5 μm.

For fiber orientation estimation from 3D data using structure tensor analysis, we advise acquiring data at the highest resolution that time permits. We recommend calculating the spatial derivatives using a filter matched to the size of the structures of interest, while ensuring that the averaging kernel is slightly larger than the structure of interest. For future work, an adaptive approach may prove fruitful. Iterating through a range of spatial derivative kernels and keeping the estimate that maximizes the orientation certainty could lead to more accurate estimates in the presence of a distribution of fiber diameters.

#### Data pre-processing

To obtain reliable FODs using structure tensor analysis we found it necessary to perform 4 corrections, similar to those found in Khan

et al. (2015). First, image intensity variation as a function of depth must be corrected as it could bias orientation estimates. Existing corrections include dividing each slice of the z-stack by the mean intensity within that slice (Khan et al., 2015), or estimating the extinction coefficient of light in the tissue (Strasters et al., 1994) and correcting each slice using this decaying exponential, both of which should result in a constant intensity profile. Here, we chose to increase the laser power as a function of tissue depth. However, additional analysis (not shown) indicates that all three methods yield similar orientation results. Our current implementation was chosen to ensure that all slices make use of the entire 8-bit intensity range, which preserves detail as well as SNR as a function of depth. Light scattering is one of the major limitations of the current technique, as it limits the tissue depth that can reasonably be imaged. Optical clearing to minimize light scattering is one possible solution, and will be a focus of future work.

The second pre-processing step, deconvolution, is necessary because PSF anisotropy will bias orientation estimates. For this, Khan et al., 2015 chose to measure and approximate the PSF with an anisotropic 3D Gaussian function, then blurred their image in the xy plane to create an image effectively convolved with an isotropic PSF. This is an appropriate approach for their analysis, as they are interested in answering questions regarding a single dominant orientation in the MR-voxel rather than the full orientation distribution. However, our analysis requires the ability to distinguish individual fibers, and necessitates deconvolution. Using the same data from the sensitivity analysis, we performed analysis without the deconvolution step (but all other parameters constant), and find a significant bias in the through plane direction, with an average of 16° angular error towards the A/P direction, or towards the third dimension (data not shown). Interestingly, the in-plane error remained minimal (<4°).

The third operation, interpolation to isotropic resolution, is necessary (as described before) to ensure that in-plane and through-plane fibers are weighted equally in the final distribution. The final correction is a simple geometric correction to account for tissue shrinkage. The thickness after histological processing was consistently found to be between 50 and 55 μm, or 62–68% of the thickness of the original section. These values, again, are in line with those obtained from Khan et al., 2015, where similar processing and staining techniques were used.

#### Conclusion

We have demonstrated the ability of structure tensor analysis to extract the 3D FOD from confocal microscopy z-stacks and compared these to FODs calculated via constrained spherical deconvolution for the same voxel locations. Agreement is good (5–11°) for both single and crossing fibers, except when the crossing angle is less than about 60°. This technique represents a considerable advancement in the development of a “gold standard” for validating fiber reconstruction methods, and could be used to assess and improve the various “crossing fiber” algorithms that attempt to recover the FOD or ODF on a voxel-wise scale. Further, by extracting features such as the spread of fiber orientations and the fractions of fibers in each direction, these methods could be the basis of detailed studies of the relationship between the diffusion MRI signal and the underlying tissue microstructure.

#### Acknowledgments

This work was supported by the National Institute of Neurological Disorders and Stroke of the National Institutes of Health under award number 2RO1NS058639-05/08 and National Institutes of Health grant 1S10 RR 17789. Whole slide imaging was performed in the Digital Histology Shared Resource at the Vanderbilt University Medical Center ([www.mc.vanderbilt.edu/dhsr](http://www.mc.vanderbilt.edu/dhsr)).

## References

- Alexander, D.C., 2005. Multiple-fiber reconstruction algorithms for diffusion MRI. *Ann. N. Y. Acad. Sci.* 1064, 113–133.
- Alexander, D.C., Pierpaoli, C., Bassier, P.J., Gee, J.C., 2001. Spatial transformations of diffusion tensor magnetic resonance images. *IEEE Trans. Med. Imaging* 20, 1131–1139.
- Anderson, A.W., 2005. Measurement of fiber orientation distributions using high angular resolution diffusion imaging. *Magn. Reson. Med.* 54, 1194–1206.
- Arseneau, S., 2006. Structure Tensor – Introduction and Tutorial. MATLAB Central File Exchange.
- Assaf, Y., Bassier, P.J., 2005. Composite hindered and restricted model of diffusion (CHARMED) MR imaging of the human brain. *NeuroImage* 27, 48–58.
- Axelsson, M., 2008. Estimating 3D Fibre Orientation in Volume Images. *Pattern Recognition*, 2008. ICPRI 2008. 19th International Conference on, pp. 1–4.
- Basser, P.J., Pierpaoli, C., 1996. Microstructural and physiological features of tissues elucidated by quantitative-diffusion-tensor MRI. *J. Magn. Reson. B* 111, 209–219.
- Basser, P.J., Mattiello, J., LeBihan, D., 1994. MR diffusion tensor spectroscopy and imaging. *Biophys. J.* 66, 259–267.
- Beaulieu, C., 2002. The basis of anisotropic water diffusion in the nervous system – a technical review. *NMR Biomed.* 15, 435–455.
- Behrns, T.E., Woolrich, M.W., Jenkinson, M., Johansen-Berg, H., Nunes, R.G., Clare, S., Matthews, P.M., Brady, J.M., Smith, S.M., 2003. Characterization and propagation of uncertainty in diffusion-weighted MR imaging. *Magn. Reson. Med.* 50, 1077–1088.
- Behrns, T.E., Berg, H.J., Jbabdi, S., Rushworth, M.F., Woolrich, M.W., 2007. Probabilistic diffusion tractography with multiple fibre orientations: what can we gain? *NeuroImage* 34, 144–155.
- Biggs, D.S., 2010. 3D deconvolution microscopy. *Curr. Protoc. Cytom.* 11–20 Chapter 12, Unit 12.19.
- Biggs, D.S.C., Andrews, M., 1997. Acceleration of iterative image restoration algorithms. *Appl. Opt.* 36, 1766–1775.
- Bigun, J., Granlund, G.H., 1987. Optimal Orientation Detection of Linear Symmetry. *Proceedings of the IEEE First International Conference on Computer Vision*, pp. 433–438.
- Bingham, C., 1974. An Antipodally Symmetric Distribution on the Sphere. pp. 1201–1225.
- Budde, M.D., Frank, J.A., 2012. Examining brain microstructure using structure tensor analysis of histological sections. *NeuroImage* 63, 1–10.
- Cai, T., Fan, J., Jiang, T., 2013. Distributions of angles in random packing on spheres. *J. Mach. Learn. Res.* 14, 1837–1864.
- Choe, A.S., Gao, Y., Li, X., Compton, K.B., Stepniewska, I., Anderson, A.W., 2011. Accuracy of image registration between MRI and light microscopy in the ex vivo brain. *Magn. Reson. Imaging* 29, 683–692.
- Choe, A.S., Stepniewska, I., Colvin, D.C., Ding, Z., Anderson, A.W., 2012. Validation of diffusion tensor MRI in the central nervous system using light microscopy: quantitative comparison of fiber properties. *NMR Biomed.* 25, 900–908.
- Daducci, A., Canales-Rodriguez, E.J., Descoteaux, M., Garyfallidis, E., Gur, Y., Lin, Y.C., Mani, M., Merlet, S., Paquette, M., Ramirez-Manzanares, A., Reisert, M., Reis Rodrigues, P., Sepehrband, F., Caruyer, E., Choupan, J., Deriche, R., Jacob, M., Menegaz, G., Prkovska, V., Rivera, M., Wiaux, Y., Thiran, J.P., 2014. Quantitative comparison of reconstruction methods for intra-voxel fiber recovery from diffusion MRI. *IEEE Trans. Med. Imaging* 33, 384–399.
- Dauguet, J., Delzecaux, T., Conde, F., Mangin, J.F., Ayache, N., Hantraye, P., Frouin, V., 2007. Three-dimensional reconstruction of stained histological slices and 3D non-linear registration with in-vivo MRI for whole baboon brain. *J. Neurosci. Methods* 164, 191–204.
- Dell'acqua, F., Scifo, P., Rizzo, G., Catani, M., Simmons, A., Scotti, G., Fazio, F., 2010. A modified damped Richardson–Lucy algorithm to reduce isotropic background effects in spherical deconvolution. *NeuroImage* 49, 1446–1458.
- Descoteaux, M., Angelino, E., Fitzgibbons, S., Deriche, R., 2007. Regularized, fast, and robust analytical Q-ball imaging. *Magn. Reson. Med.* 58, 497–510.
- Descoteaux, M., Deriche, R., Knosche, T.R., Anwander, A., 2009. Deterministic and probabilistic tractography based on complex fibre orientation distributions. *IEEE Trans. Med. Imaging* 28, 269–286.
- Eltoum, I., Fredenburgh, J., Myers, R.B., Grizzle, W.E., 2001. Introduction to the theory and practice of fixation of tissues. *J. Histotechnol.* 24, 173–190.
- Farrher, E., Kaffanke, J., Celik, A.A., Stöcker, T., Grinberg, F., Shah, N.J., 2012. Novel multisection design of anisotropic diffusion phantoms. *Magn. Reson. Imaging* 30, 518–526.
- Ferizi, Z., Schneider, T., Tariq, M., Wheeler-Kingshott, C.M., Zhang, H., Alexander, D., 2013. The Importance of Being Dispersed: A Ranking of Diffusion MRI Models for Fibre Dispersion Using In Vivo Human Brain Data. In: Mori, K., Sakuma, I., Sato, Y., Barillot, C., Navab, N. (Eds.), *Medical Image Computing and Computer-Assisted Intervention – MICCAI 2013*. Springer, Berlin Heidelberg, pp. 74–81.
- Fieremans, E., De Deene, Y., Delpetite, S., Ozdemir, M.S., Achten, E., Lemahieu, I., 2008. The design of anisotropic diffusion phantoms for the validation of diffusion weighted magnetic resonance imaging. *Phys. Med. Biol.* 53, 5405–5419.
- Hagmann, P., Kurant, M., Gigandet, X., Thiran, P., Wedeen, V.J., Meuli, R., Thiran, J.-P., 2007. Mapping human whole-brain structural networks with diffusion MRI. *PLoS One* 2, e597.
- Harris, C., Stephens, M., 1988. A Combined Corner and Edge Detector. *Proc. Alvey Vision Conf.* 147–151.
- Hong, X., Arlinghaus, L.R., Anderson, A.W., 2009. Spatial normalization of the fiber orientation distribution based on high angular resolution diffusion imaging data. *Magn. Reson. Med.* 61, 1520–1527.
- Jansons, K.M., Alexander, D.C., 2003. Persistent angular structure: new insights from diffusion MRI data. Dummy version. *Inf. Process. Med. Imaging* 18, 672–683.
- Jespersen, S.N., Leigland, L.A., Cornea, A., Kroenke, C.D., 2012. Determination of axonal and dendritic orientation distributions within the developing cerebral cortex by diffusion tensor imaging. *IEEE Trans. Med. Imaging* 31, 16–32.
- Jones, D.K., 2004. The effect of gradient sampling schemes on measures derived from diffusion tensor MRI: a Monte Carlo study. *Magn. Reson. Med.* 51, 807–815.
- Jones, D.K., Horsfield, M.A., Simmons, A., 1999. Optimal strategies for measuring diffusion in anisotropic systems by magnetic resonance imaging. *Magn. Reson. Med.* 42, 515–525.
- Khan, A.R., Cornea, A., Leigland, L.A., Kohama, S.G., Jespersen, S.N., Kroenke, C.D., 2015. 3D structure tensor analysis of light microscopy data for validating diffusion MRI. *NeuroImage* 111, 192–203.
- Kitamura, S., Kiuchi, K., Taoka, T., Hashimoto, K., Ueda, S., Yasuno, F., Morikawa, M., Kichikawa, K., Kishimoto, T., 2013. Longitudinal white matter changes in Alzheimer's disease: a tractography-based analysis study. *Brain Res.* 1515, 12–18.
- Koenig, K.A., Sakaie, K.E., Lowe, M.J., Lin, J., Stone, L., Bermel, R.A., Beall, E.B., Rao, S.M., Trapp, B.D., Phillips, M.D., 2015. The relationship between cognitive function and high-resolution diffusion tensor MRI of the cingulum bundle in multiple sclerosis. *Mult. Scler. J.* 1–8.
- Köthe, U., 2003. Edge and Junction Detection with an Improved Structure Tensor. In: Michaelis, B., Krell, G. (Eds.), *Pattern Recognition*. Springer, Berlin Heidelberg, pp. 25–32.
- Krause, M., Hausherr, J.M., Burgeth, B., Herrmann, C., Krenkel, W., 2010. Determination of the fibre orientation in composites using the structure tensor and local X-ray transform. *J. Mater. Sci.* 45, 888–896.
- Leergaard, T.B., White, N.S., de Crespigny, A., Bolstad, I., D'Arceuil, H., Bjaalie, J.G., Dale, A.M., 2010. Quantitative histological validation of diffusion MRI fiber orientation distributions in the rat brain. *PLoS One* 5, e8595.
- Lin, C.-P., Wedeen, V.J., Chen, J.-H., Yao, C., Tseng, W.-Y.I., 2003. Validation of diffusion spectrum magnetic resonance imaging with manganese-enhanced rat optic tracts and ex vivo phantoms. *NeuroImage* 19, 482–495.
- Mori, S., van Zijl, P.C.M., 2002. Fiber tracking: principles and strategies – a technical review. *NMR Biomed.* 15, 468–480.
- Mori, S., Crain, B.J., Chacko, V.P., van Zijl, P.C., 1999. Three-dimensional tracking of axonal projections in the brain by magnetic resonance imaging. *Ann. Neurol.* 45, 265–269.
- Nilsson, M., Latt, J., Stahlberg, F., van Westen, D., Hagslatt, H., 2012. The importance of axonal undulation in diffusion MR measurements: a Monte Carlo simulation study. *NMR Biomed.* 25, 795–805.
- Ozarslan, E., Shepherd, T.M., Vemuri, B.C., Blackband, S.J., Mareci, T.H., 2006. Resolution of complex tissue microarchitecture using the diffusion orientation transform (DOT). *NeuroImage* 31, 1086–1103.
- Pawley, J.B., Masters, R.B.R., 1996. *Handbook of Biological Confocal Microscopy*, Second Edition. Opt. Eng. 35, 2765–2766.
- Perrin, M., Poupon, C., Rieul, B., Leroux, P., Constantinesco, A., Mangin, J.F., Lebihan, D., 2005. Validation of q-ball imaging with a diffusion fibre-crossing phantom on a clinical scanner. *Philos. Trans. R. Soc. Lond. Ser. B Biol. Sci.* 360, 881–891.
- Rohde, G.K., Aldroubi, A., Dawant, B.M., 2003. The adaptive bases algorithm for intensity-based nonrigid image registration. *IEEE Trans. Med. Imaging* 22, 1470–1479.
- Sakai, K.E., Lowe, M.J., 2007. An objective method for regularization of fiber orientation distributions derived from diffusion-weighted MRI. *NeuroImage* 34, 169–176.
- Seehaus, A.K., Roebroeck, A., Chiry, O., Kim, D.S., Ronen, I., Bratzke, H., Goebel, R., Galuske, R.A., 2013. Histological validation of DW-MRI tractography in human postmortem tissue. *Cereb. Cortex* 23, 442–450.
- Seehaus, A., Roebroeck, A., Bastiani, M., Fonseca, L., Bratzke, H., Lori, N., Vilanova, A., Goebel, R., Galuske, R., 2015. Histological validation of high-resolution DTI in human post mortem tissue. *Front. Neuroanat.* 9, 98.
- Shenton, M.E., Hamoda, H.M., Schneiderman, J.S., Bouix, S., Pasternak, O., Rathi, Y., M-A.V., Purohit, M.P., Helmer, K., Koerte, I., Lin, A.P., C-F.W., Kikinis, R., Kubicki, M., Stern, R.A., Zafonte, R., 2012. A review of magnetic resonance imaging and diffusion tensor imaging findings in mild traumatic brain injury. *Brain Imaging Behav.* 6, 137–192.
- Singh, M., Rajagopalan, A., Kim, T.S., Hwang, D., Chui, H., Zhang, X.L., Lee, A.Y., Zarow, C., 2008. Co-registration of in-vivo human MRI brain images to postmortem histological microscopic images. *Int. J. Imaging Syst. Technol.* 18, 325–335.
- Sotiropoulos, S.N., Behrens, T.E., Jbabdi, S., 2012. Ball and rackets: inferring fiber fanning from diffusion-weighted MRI. *NeuroImage* 60, 1412–1425.
- Strasters, K.C., van der Voort, H.T.M., Geusebroek, J.M., Smeulders, A.W.M., 1994. Fast attenuation correction in fluorescence confocal imaging: a recursive approach. *Bioimaging* 2, 78–92.
- Tariq, M., Schneider, T., Alexander, D., Wheeler-Kingshott, C.M., Zhang, H., 2014. In Vivo Estimation of Dispersion Anisotropy of Neurites Using Diffusion MRI. In: Golland, P., Hata, N., Barillot, C., Hornegger, J., Howe, R. (Eds.), *Medical Image Computing and Computer-assisted Intervention – MICCAI 2014*. Springer International Publishing, pp. 241–248.
- Toga, A.W., Ambach, K.L., Schluender, S., 1994. High-resolution anatomy from in situ human brain. *NeuroImage* 1, 334–344.
- Tournier, J.D., Calamante, F., Gadian, D.G., Connelly, A., 2004. Direct estimation of the fiber orientation density function from diffusion-weighted MRI data using spherical deconvolution. *NeuroImage* 23, 1176–1185.
- Tournier, J.D., Calamante, F., Connelly, A., 2007. Robust determination of the fibre orientation distribution in diffusion MRI: non-negativity constrained super-resolved spherical deconvolution. *NeuroImage* 35, 1459–1472.
- Tuch, D.S., 2004. Q-ball imaging. *Magn. Reson. Med.* 52, 1358–1372.
- Tuch, D.S., Reese, T.G., Wiegell, M.R., Makris, N., Belliveau, J.W., Wedeen, V.J., 2002. High angular resolution diffusion imaging reveals intravoxel white matter fiber heterogeneity. *Magn. Reson. Med.* 48, 577–582.
- Wang, H., Lenglet, C., Akkin, T., 2015. Structure tensor analysis of serial optical coherence scanner images for mapping fiber orientations and tractography in the brain. *J. Biomed. Opt.* 20, 036003.
- Wedeen, V.J., Hagmann, P., Tseng, W.Y., Reese, T.G., Weisskoff, R.M., 2005. Mapping complex tissue architecture with diffusion spectrum magnetic resonance imaging. *Magn. Reson. Med.* 54, 1377–1386.

- Wehrl, H.F., Bezrukov, I., Wiehr, S., Lehnhoff, M., Fuchs, K., Mannheim, J.G., Quintanilla-Martinez, L., Kohlhofer, U., Kneilling, M., Pichler, B.J., Sauter, A.W., 2015. Assessment of murine brain tissue shrinkage caused by different histological fixatives using magnetic resonance and computed tomography imaging. *Histol. Histopathol.* 30, 601–613.
- Westin, C.F., Maier, S.E., Mamata, H., Nabavi, A., Jolesz, F.A., Kikinis, R., 2002. Processing and visualization for diffusion tensor MRI. *Med. Image Anal.* 6, 93–108.
- White, T., Nelson, M., Lim, K.O., 2008. Diffusion tensor imaging in psychiatric disorders. *Top. Magn. Reson. Imaging* 19, 97–109.
- Wiegell, M.R., Larsson, H.B., Wedeen, V.J., 2000. Fiber crossing in human brain depicted with diffusion tensor MR imaging. *Radiology* 217, 897–903.
- Williams, J.H., Mepham, B.L., Wright, D.H., 1997. Tissue preparation for immunocytochemistry. *J. Clin. Pathol.* 50, 422–428.
- Woods, A.E., E.R., 1994. *Laboratory Histopathology*. Churchill Livingstone, New York.
- Yanasak, N., Allison, J., 2006. Use of capillaries in the construction of an MRI phantom for the assessment of diffusion tensor imaging: demonstration of performance. *Magn. Reson. Imaging* 24, 1349–1361.
- Zhang, H., Schneider, T., Wheeler-Kingshott, C.A., Alexander, D.C., 2012. NODDI: practical *in vivo* neurite orientation dispersion and density imaging of the human brain. *NeuroImage* 61, 1000–1016.